Applied Surface Science 746 (2026) 167591

Contents lists available at ScienceDirect

Applied Surface Science

journal homepage: www.elsevier.com/locate/apsusc

Full Length Article

Interfacial engineering of Cu-Au core-nanocluster systems for oxygen reduction, reactive oxygen species generation, and antimicrobial activity

Patrick Irigo [a,1], Ya Li [b,1], Tong Liu [b,1], Etelka Chung [a,1], Yujia Luo [c], Xiangqun Zhuge [b], Miriam Roldán-Matilla [d], Arisbel Cerpa-Naranjo [e], Isabel Lado-Touriño [e,**], Kun Luo [b,*], María F. Gilsanz-Muñoz [e,f], Guogang Ren [a,**]

[a] School of Engineering and Computer Science, University of Hertfordshire, AL10 9AB, UK
[b] School of Materials Science and Engineering, Changzhou University, Changzhou 213164, PR China
[c] The First Affiliated Hospital, School of Medicine, Zhejiang University, Hangzhou 310003, PR China
[d] Professional Formation Centre, European University of Madrid, Villaviciosa de Odón, 28670 Madrid, Spain
[e] Department of Engineering, School of Architecture, Engineering, Science and Computing, European University of Madrid, Villaviciosa de Odón, 28670 Madrid, Spain
[f] Department of Science, Computing and Technology, European University of Madrid, Villaviciosa de Odón, 28670 Madrid, Spain

ARTICLE INFO

Keywords:
Cu-Au core-nanocluster nanoparticles
Oxygen reduction reaction
Reactive oxygen species
Galvanic corrosion
Interfacial catalysis
Antimicrobial activity

ABSTRACT

Cu-Au core-nanocluster nanoparticles (NPs) offer a promising platform for multifunctional antimicrobial materials through coupled oxygen reduction, reactive oxygen species (ROS) generation, and galvanically enhanced ion release. Here, the interfacial mechanisms governing antimicrobial activity in $CuAu_x$ NPs are investigated using structural characterisation, density functional theory (DFT), electrochemical analysis, and antibacterial testing. SEM, TEM, XRD, and XPS confirm a Cu-Au core-nanocluster architecture comprising ~ 50 nm Cu NPs decorated with ~ 2–3 nm Au nanoclusters, generating abundant catalytic interfacial sites. DFT calculations reveal complementary roles for Cu and Au, whereby Cu promotes oxygen activation by reducing the O–O dissociation barrier to 0.189 eV, while Au stabilises partially reduced intermediates and favours selective two-electron oxygen reduction. Rotating ring-disk electrode measurements validate H_2O_2 generation, while chronoamperometry demonstrates stable electrochemical performance. Galvanic Cu^{2+} release reaches 2442.67 μg/mL (73.28% dissolution) under acidic conditions, with physical-mixture controls confirming the importance of intimate Cu-Au coupling. Antibacterial assays identify $CuAu_{1.5}$ as the optimal composition, exhibiting the highest inhibition against *E. coli* (~1.0 cm) and *S. aureus* (~1.4–1.5 cm). The results establish a direct structure–property-performance relationship linking Cu-Au interfacial architecture to oxygen reduction, ROS generation, Cu^{2+} release, and antimicrobial activity, highlighting interfacial engineering as an effective strategy for antimicrobial nanomaterial design.

1. Introduction

Metallic nanomaterials have attracted considerable interest for antimicrobial applications because their high surface area and tuneable electronic properties enable multiple antibacterial pathways, including metal-ion release, reactive oxygen species (ROS) generation, and membrane disruption [1–3]. Compared with conventional antimicrobial agents, nanostructured metals can provide sustained activity through surface-mediated physicochemical interactions while reducing the likelihood of resistance development [4,5]. Among these mechanisms, catalytic ROS generation has emerged as a particularly attractive strategy because it enables continuous production of oxidative species through interfacial redox reactions rather than relying solely on passive ion release [6,7]. However, the relationship between nanoscale

* Corresponding author at: University of Hertfordshire, Hatfield, Herts AL10 9AB, UK.
** Corresponding author.
E-mail addresses: p.irigo2@herts.ac.uk (P. Irigo), 3479244242@qq.com (Y. Li), liutonguse@qq.com (T. Liu), e.chung@herts.ac.uk (E. Chung), yujialuo@zju.edu.cn (Y. Luo), zgxq@cczu.edu.cn (X. Zhuge), miriam.roldan@universidadeuropea.es (M. Roldán-Matilla), arisbel.cerpa@universidadeuropea.es (A. Cerpa-Naranjo), misabel.lado@universidadeuropea.es (I. Lado-Touriño), luokun@cczu.edu.cn (K. Luo), mariafuencisla.gilsanz@universidadeuropea.es (M.F. Gilsanz-Muñoz), g.g.ren@herts.ac.uk (G. Ren).
[1] Authors with equal contributions as first authors.

https://doi.org/10.1016/j.apsusc.2026.167591
Received 1 April 2026; Received in revised form 7 June 2026; Accepted 17 June 2026
Available online 23 June 2026

structure, interfacial chemistry, and the coupled processes governing ion release, oxygen reduction, and ROS generation remains insufficiently understood.

Copper (Cu)-based nanomaterials are widely recognised for their broad-spectrum antimicrobial activity, arising primarily from Cu^{+}/Cu^{2+} release and redox-mediated ROS formation [3,8,9]. Their effectiveness generally increases with decreasing particle size owing to enhanced surface reactivity and ion release kinetics [8,10]. Nevertheless, Cu-based systems often suffer from rapid oxidation, uncontrolled dissolution behaviour, and limited selectivity in oxygen reduction pathways, which can compromise both stability and long-term performance [11–13]. In contrast, gold (Au) nanostructures exhibit excellent chemical stability together with well-defined catalytic and electronic properties [14–16]. Although Au possesses limited intrinsic antimicrobial activity, its ability to modify local electronic structure and catalytic behaviour makes it an attractive component for multifunctional antimicrobial systems [17–19].

Bimetallic Cu-Au nanostructures provide a promising route to integrate the complementary properties of both metals. Electronic coupling between Cu and Au can alter adsorption energetics, facilitate charge transfer, and enhance oxygen reduction reactions (ORR) [20–22]. Previous studies have demonstrated high selectivity towards hydrogen peroxide (H_2O_2) generation through a two-electron ORR pathway, highlighting the importance of Cu-Au interfacial sites in controlling reaction pathways and catalytic efficiency [21,23]. Because H_2O_2 acts both as a direct antimicrobial agent and as a precursor to more reactive oxygen species, selective ORR-driven H_2O_2 generation offers a promising strategy for enhancing antimicrobial activity [24–26]. However, it remains unclear whether the enhanced performance of Cu-Au systems arises simply from combining Cu and Au components or from the formation of electronically coupled interfacial sites capable of fundamentally altering reaction pathways. Consequently, the mechanistic relationship between interfacial structure, oxygen reduction, ROS generation, and antimicrobial activity remains poorly understood.

To address this challenge, $CuAu_x$ core-nanocluster nanostructures were designed in which ultrasmall Au nanoclusters (<3 nm) are selectively distributed across a Cu NP core, generating a high density of accessible Cu-Au interfacial sites. Unlike conventional core–shell architectures, this configuration preserves both exposed Cu domains and catalytically active Au nanoclusters, enabling simultaneous Cu dissolution and oxygen reduction. The resulting galvanic coupling promotes electron transfer from Cu to Au, facilitating oxygen activation and sustained ROS generation [21,27,28]. DFT calculations predict that these interfacial sites enhance charge transfer, reduce oxygen activation barriers, and favour selective two-electron ORR pathways for H_2O_2 formation [23,29–31]. In addition, the Au nanoclusters provide plasmonic functionality that may further enhance antimicrobial activity under illumination through local photothermal heating [32–35].

In this work, $CuAu_x$ core-nanocluster nanostructures were systematically investigated to establish direct structure–property-performance relationships governing antimicrobial activity. Structural characterisation, first-principles calculations, electrochemical measurements, and antibacterial assays were combined to evaluate how Cu-Au interfacial architecture influences oxygen reduction, Cu^{2+} release, and ROS generation. Particular emphasis was placed on distinguishing the role of electronically coupled interfacial sites from that of physically mixed Cu and Au components. The results demonstrate that antimicrobial activity is governed primarily by the density and accessibility of Cu-Au interfacial sites, which promote selective oxygen reduction and coupled Cu dissolution, while photothermal effects provide a secondary enhancement under illumination. These findings establish interfacial engineering as a rational strategy for designing multifunctional antimicrobial nanomaterials with enhanced catalytic and antibacterial performance.

2. Materials and Methods

2.1. Materials and Nanoparticle Synthesis

2.1.1. Synthesis of Cu NPs

Cu NPs were synthesised via chemical reduction. KOH (22.4 g) and $NaBH_4$ (2.7 g) were dissolved in 200 mL deionised water, followed by the addition of EDTA (8 g) and PVP (8 g). The mixture was stirred at 40 °C until complete dissolution, after which 200 mL of 0.8 mol/L $CuSO_4$ solution was added dropwise (50 drops/min) under vigorous stirring. Following 30 min of reaction and 1 h ageing, the suspension was centrifuged (12,000 rpm, 30 min), washed repeatedly with deionised water to neutral pH, rinsed with ethanol, and freeze-dried.

2.1.2. Synthesis of Cu-Au Core-Nanoclusters

$CuAu_x$ NPs were synthesised through galvanic displacement by decorating pre-synthesised Cu NPs with Au nanoclusters. Briefly, 28.8 mg Cu NPs was dispersed in 10 mL ethanol, followed by dropwise addition of $HAuCl_4$ and mercaptosuccinic acid (MSA) solutions under magnetic stirring at room temperature. After 2 h, the products were recovered by centrifugation (12,000 rpm, 13,820 × g), washed with deionised water and ethanol, and freeze-dried. The $CuAu_{1.5}$ composition (Cu ≈ 1:10) was selected as the optimised formulation for subsequent investigation. $CuAu_1$ and $CuAu_2$ variants were prepared using proportionally lower and higher $HAuCl_4$/MSA concentrations, respectively. Pristine Au nanoclusters were synthesised by $NaBH_4$ reduction of $HAuCl_4$ in the presence of MSA, purified by dialysis for 7 days, and freeze-dried.

2.1.3. Surface treatments of NPs

To evaluate the influence of environmental conditioning on antimicrobial performance, NP slurries were treated in 3.5% NaCl, 0.9% NaCl, 3% PVP, or a combined 3.5% NaCl/3% PVP solution under stirring (500 rpm, 1.5 h). The treated NPs were recovered by centrifugation, washed with deionised water and ethanol, and vacuum-dried prior to testing.

2.2. Structural and surface characterisation

The morphology and microstructure of the synthesised NPs were characterised using field-emission scanning electron microscopy (Phenom LE, Thermo Fisher Scientific) and high-resolution transmission electron microscopy (JEM-2100, JEOL). Crystalline phase composition was analysed by X-ray diffraction (D/max 2500PC, Rigaku) using Cu Kα radiation (λ = 1.5406 Å), while surface elemental composition was examined by X-ray photoelectron spectroscopy (ESCALAB 250Xi, Thermo Fisher Scientific). SEM and TEM were used to evaluate particle morphology, particle size distribution, and nanoscale architecture, whereas XRD and XPS were employed to identify crystalline phases and confirm the presence of Cu, Au, O, and C species within the Cu-Au core-nanocluster system.

2.3. Electrochemical characterisation

Electrochemical measurements were performed using a CHI760 electrochemical workstation in O_2-saturated 0.1 M KOH employing a conventional three-electrode configuration consisting of a catalyst-modified glassy carbon working electrode, Ag/AgCl reference electrode, and Pt wire counter electrode. Chronoamperometric measurements were conducted at a constant potential of −0.1 V to evaluate the electrochemical durability of the Cu-Au catalysts during continuous oxygen reduction. Rotating ring-disk electrode (RRDE) measurements were performed using an ALS RRDE-3A system (BAS) equipped with a 4 mm glassy carbon disk and Pt ring electrode. Catalyst ink (8 μL) was deposited onto the disk electrode and measurements were conducted at a scan rate of 10 mV/s. The electron transfer number and H_2O_2 yield were calculated from the disk and ring currents to evaluate oxygen

reduction selectivity and ROS precursor generation.

2.4. Antimicrobial Assay

Stock cultures of *E. coli* and *S. aureus* grown on nutrient agar, were cultured and diluted in corresponding broths to achieve desired concentrations. Microbial cell densities were adjusted to ~ 3×10^7 CFU/mL using spectrophotometric absorbance at 600 nm (0.1 OD for bacterial cells) and spread onto Mueller-Hinton agar (Sigma-Aldrich, Dorset, UK). Wells (4 mm diameter) were created using a cork borer, and 1000 μg/mL NP suspensions were pipetted into the wells. Plates were incubated at 37 °C for 24 h, after which the zone of inhibition was measured in cm. Each sample was tested in triplicate, and the mean results were calculated.

2.5. Computational modelling

2.5.1. DFT modelling of ORR and ROS generation

ROS generation on Au- and Cu-based nanomaterials was investigated using DFT calculations performed with BIOVIA Materials Studio. Although the experimental systems involve Au nanoclusters (2–3 nm) and Cu NPs (≈40 nm), DFT calculations employ periodic slab models to represent the local surface chemistry and active sites responsible for oxygen activation, rather than explicitly modelling entire NPs [31]. All calculations were carried out using the GGA-PW91 functional [36] as implemented in the DMol^3 code [37], with a double numerical plus polarization (DNP) basis set and a cutoff energy of 0.1 eV per atom [38]. Core electrons were treated using DFT semi-core pseudopotentials. A 5 × 5 × 1 k-point mesh was used for Brillouin zone integration [39]. Geometry optimizations employed strict convergence criteria, with an energy gradient threshold of 2.7×10^{-4} eV, a maximum force of 0.054 eV Å^{-1}, and a maximum atomic displacement of 0.005 Å. A thermal smearing of 0.2 eV and dipole slab corrections were applied to ensure convergence and eliminate spurious electrostatic interactions.

Metal surfaces were modelled using periodic (2 × 2) fcc(111) slabs consisting of four atomic layers separated by a 20 Å vacuum region. The bottom two layers were fixed, while the top two layers were fully relaxed. To examine the effect of Cu incorporation, three surface configurations were considered: an Au(111) surface containing a single Cu atom substituted in the outermost layer, an Au(111) slab containing one Cu subsurface layer beneath the Au surface, and an Au(111) slab containing two Cu subsurface layers beneath the Au surface (Fig. 1). These models represent increasing Cu enrichment rather than fixed stoichiometric ratios. Adsorbates relevant to the oxygen reduction reaction were placed at high-symmetry adsorption sites identified within the (2 × 2) surface unit cell, and reaction free energies were calculated using the computational hydrogen electrode approach. Transition states were identified using the complete Linear/Quadratic Synchronous Transit (LST/QST) method.

2.5.2. Photothermal and plasmonic simulations

Photothermal simulations were performed to investigate the influence of Au cluster coverage on heat generation in $CuAu_x$ core-nanocluster systems. Finite-difference time-domain (FDTD) simulations were first used to calculate the optical absorption of individual NPs with Au coverages of 0%, 15%, 25%, and 35% under irradiation at λ = 580 nm and an incident irradiance of 100 mW/cm. Structural parameters, including the average NP diameter (53.8 Å ± 6.5 nm) and Au nanocluster size (~2–3 nm), were based on TEM characterisation.

To evaluate collective photothermal behaviour, the $CuAu_{1.5}$ configuration (25% Au coverage) was modelled as a 3 × 3 NP array with interparticle spacings of 100–200 nm. Simulations were performed on a PVDF substrate to assess plasmonic coupling and heat confinement under practical coating conditions [40]. Steady-state thermal analysis was conducted at 25 °C assuming negligible convection and phase change effects [33].

The thermal power generated by an individual NP was calculated from its absorption cross-section (C_{abs}) and incident irradiance (I_0) [41,42]:

$$Q_{single} = C_{abs} I \tag{1}$$

To evaluate the resulting thermal behaviour, steady-state heat diffusion simulations were performed in ANSYS Fluent [43,44]. The specific absorption rate (SAR, W/m^3) of the NP ensemble is then evaluated to quantify total photothermal energy deposition per unit volume:

$$SAR = Q_{total} = \sum Q_{single} = n C_{abs} I \tag{2}$$

This term defines the collective heat source (Q_{total}) for subsequent modelling of temperature dynamics, where n represents the NP surface density. The collective photothermal response of the NP-laden system was calculated using the heat diffusion equation accounting for both localised and bulk heating:

$$\rho c_p \frac{\partial T}{\partial t} = \kappa \nabla^2 T + Q_{total} \tag{3}$$

where ρ is the material density, c_p is the specific heat capacity, κ is the thermal conductivity, these parameters summarised in Table 1 govern

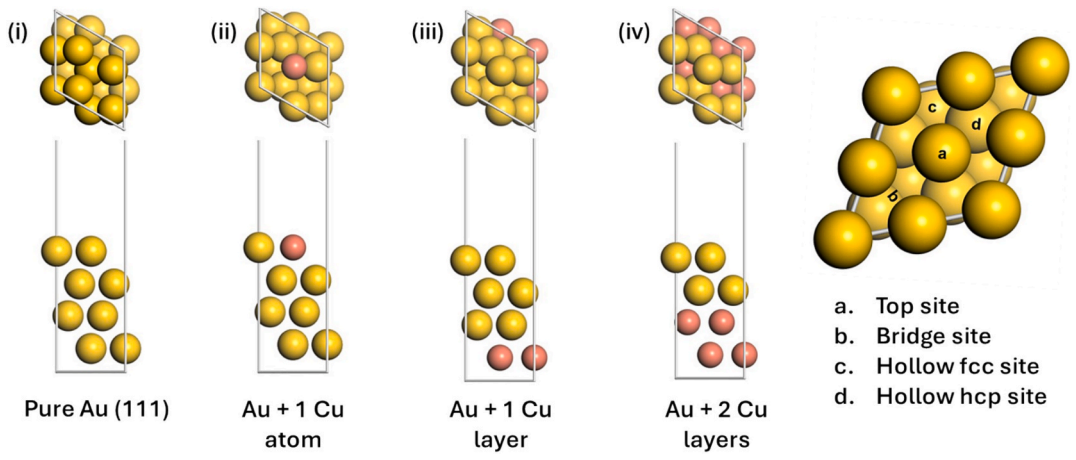

Fig. 1. Top and side views of the Au(111) slab models used for the DFT calculations, illustrating progressive Cu incorporation within the Au lattice: (i) pristine Au (1 1 1), (ii) Au(1 1 1) containing a single Cu atom substituted into the outermost surface layer, (iii) Au(1 1 1) containing one Cu subsurface layer beneath the Au surface, and (iv) Au(1 1 1) containing two Cu subsurface layers beneath the Au surface. The schematic on the right shows the (2 × 2) surface unit cell and the symmetry-distinct adsorption sites considered for ORR intermediates, including the top, bridge, hollow fcc, and hollow hcp sites.

Table 1
Thermal properties of materials used in the photothermal heat transfer model.

Material	ρ(kg/m^3)	c_p(J/kg·K)	κ(W/m·K)	Ref
Au	19,300	129	318	[45]
Cu	8,960	385	400	[45]
PVDF	1,380	1000	0.28	[46]
Air	1.225	1006.43	0.026	[47]

how NP-derived heat generation (Eq. (3) propagates through the system, enabling prediction of microbial inactivation thresholds from transient surface temperatures.

3. Results and Discussion

3.1. Structural basis of the Cu-Au Core-Nanocluster system

The structural and compositional characteristics of the Cu-Au core-nanocluster system were investigated using SEM, TEM, XRD, and XPS (Fig. 2). SEM analysis (Fig. 2a) reveals Cu NPs with diameters predominantly between 50 and 60 nm, providing a high-surface-area scaffold for Au nanocluster deposition. TEM analysis (Fig. 2b) confirms the formation of ultrasmall Au nanoclusters with characteristic dimensions of approximately 2–3 nm and a lattice spacing of 0.232 nm corresponding to the Au(1 1 1) plane. The assembled $CuAu_{1.5}$ structure (Fig. 2c) exhibits a heterogeneous architecture in which Au nanoclusters are distributed across the Cu NP surface, generating a high density of discrete Cu-Au interfacial sites.

Unlike conventional core–shell or physically mixed Cu/Au systems, this architecture simultaneously preserves exposed Cu domains and catalytically active Au nanoclusters, maximising interfacial contact while maintaining accessibility for both Cu dissolution and oxygen reduction. Such nanoscale junctions are expected to govern electron transfer, galvanic coupling, and oxygen reduction behaviour, as demonstrated by the DFT analyses presented in Sections 3.2.1-3.2.3 and the experimental validation discussed in Section 3.3. The intimate coupling between Cu and Au domains therefore provides the structural basis for the ROS-generation mechanism investigated in this work.

XRD analysis (Fig. 2d) confirms the coexistence of Cu-, Cu_2O-, and Au-related crystalline phases, indicating retention of distinct metallic domains rather than bulk alloy formation. The presence of Cu_2O suggests partial surface oxidation of Cu, which may influence interfacial redox behaviour during oxygen reduction. Consistent with these observations, the XPS survey spectrum (Fig. 2e) confirms the presence of Cu, Au, O, and C species within the material. Together, these results provide direct experimental evidence for the formation of abundant Cu-Au catalytic interfaces. As these interfaces are expected to govern oxygen activation, charge transfer, and ROS generation, their catalytic role was subsequently investigated using first-principles calculations. The resulting structure–property relationships underpin the catalytic, electrochemical, photothermal, and antimicrobial behaviour discussed throughout Sections 3.2-3.5.

3.2. Interfacial catalysis of ORR and ROS generation

3.2.1. ORR thermodynamics at Cu-Au interfaces

To elucidate the origin of the enhanced antimicrobial activity observed for $CuAu_{1.5}$, the thermodynamics of oxygen reduction were investigated using DFT models representing local Cu-Au catalytic interfaces. The most stable adsorption configurations of key ORR intermediates (O_2, O + O, OOH, O + OH, and H_2O_2) were identified by optimisation of adsorbate–surface interactions, with representative structures shown in Fig. S1. These models are consistent with the experimentally validated core-nanocluster architecture shown in Fig. 2 and the Cu-Au interfacial morphology identified by TEM and XPS analysis in Section 3.1, enabling direct evaluation of local catalytic behaviour rather than bulk alloy or physically mixed systems.

Adsorption energetics vary markedly with local surface composition (Table 2). Au(111) exhibits weak O_2 adsorption and limited activation, whereas Cu-containing surfaces promote substantially stronger adsorption and dissociation of O_2 and OOH intermediates. In contrast, a single subsurface Cu layer produces only minor deviations from pristine Au (111), indicating limited influence on surface reactivity. The calculated

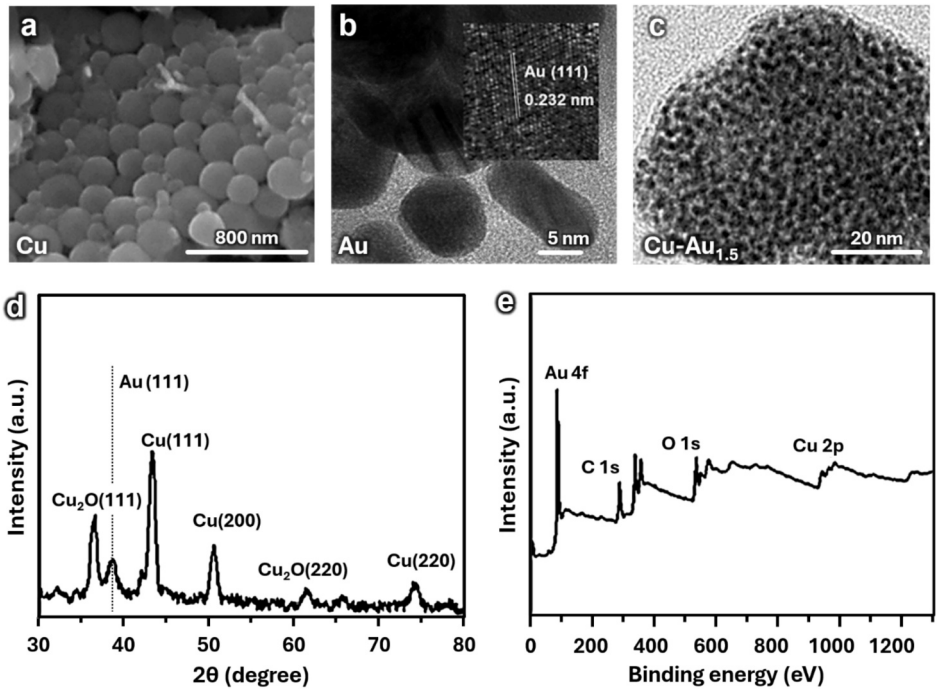

Fig. 2. Structural characterisation of the Cu-Au core-nanocluster system. (a) SEM image of Cu NPs (50–60 nm). (b) TEM image of Au nanoclusters showing the Au (111) lattice fringe with an interplanar spacing of 0.232 nm. (c) TEM image of the assembled $CuAu_{1.5}$ nanostructure. (d) XRD pattern confirming the coexistence of Cu, Cu_2O, and Au crystalline phases. (e) XPS survey spectrum confirming the presence of Cu, Au, O, and C species.

Table 2
Calculated free energies of formation (eV) for key ORR intermediates on Au, Cu, and Cu-modified Au(111) surfaces. Cu-containing surfaces enhance adsorption and activation of O_2 and OOH intermediates, while Au-rich environments stabilise partially reduced species such as H_2O_2, supporting complementary interfacial catalytic roles.

Reaction	Au	Cu	Au + 1 Cu atom	Au + 1 Cu inner layer	Au + 2 Cu inner layers
O_2 adsorption	0.332	−0.511	−0.418	0.424	−0.034
O_2 dissociation	0.731	−1.453	−0.992	–	−0.245
OOH adsorption	−0.117	−0.793	−1.039	–	−0.419
OOH dissociation	−0.673	−2.435	−2.024	–	−1.582
H_2O_2 formation	−0.816	−2.666*	−0.462	–	−0.921

*Entries marked "–" indicate cases where further calculations were not performed due to minimal deviation from pristine Au(111) behaviour·H_2O_2 dissociates into two OH groups on the Cu(111) surface; no adsorption observed due to dissociation.

energetics further reveal complementary catalytic roles for Cu- and Au-rich domains. Cu-rich sites favour O–O bond activation and intermediate dissociation, while Au-rich environments stabilise partially reduced species, particularly H_2O_2. Although Cu(111) promotes complete H_2O_2 dissociation, Au and Au + 2 Cu layer configurations preserve H_2O_2 as a stable intermediate, highlighting the importance of balancing oxygen activation and intermediate stabilisation.

Collectively, these results support a cooperative catalytic mechanism in which Cu-rich domains drive oxygen activation while adjacent Au-rich regions preserve ROS-generating intermediates (Figs. S2-S4). This synergistic behaviour promotes sustained H_2O_2 formation, central to the experimentally validated ROS-generation pathway discussed in Section 3.3 and the antimicrobial activity observed in Section 3.5. To understand the electronic origin of these adsorption trends, charge-transfer behaviour and electronic structure modifications were subsequently analysed.

3.2.2. *Charge transfer and electronic structure*

The catalytic behaviour of Cu-Au systems is governed by electronic interactions between surface atoms and adsorbed oxygen species. Mulliken charge analysis (Fig. 3) reveals an oscillatory charge-transfer profile throughout the ORR pathway, with the greatest charge transfer occurring for dissociated intermediates and the lowest values associated with intact O–O bonds. The magnitude of charge transfer follows the trend: Cu > Au + 1 Cu atom > Au + 2 Cu layers > Au which closely mirrors the adsorption strengths and reaction energetics reported in Table 2.

The nature of the adsorbed oxygen species evolves with local electronic structure. Cu(111) and Au + 1 Cu atom surfaces favour peroxo-like intermediates, whereas Au(111) and Au + 2 Cu layer surfaces preferentially stabilise superoxo species [21,23]. This behaviour is consistent with the projected density of states analysis, where Cu incorporation shifts the d-band centre towards the Fermi level, increasing orbital overlap between surface d-states and oxygen-derived orbitals. The resulting Cu-Au d-state hybridisation strengthens adsorbate binding and facilitates charge transfer into antibonding O–O orbitals, thereby promoting oxygen activation while preserving ROS-generating intermediates [15,22].

The charge-transfer trends observed in Fig. 3 closely follow the d-band shifts shown in Fig. 4, indicating that the enhanced reactivity of Cu-containing surfaces originates primarily from electronic structure modulation rather than geometric effects. This prediction is consistent with the RRDE measurements presented in Section 3.3, which experimentally confirm selective H_2O_2 generation through a predominantly two-electron oxygen reduction pathway.

To distinguish electronic effects from structural contributions, lattice parameters were analysed for all models (Table 3). Only minor lattice contraction was observed following Cu incorporation, particularly for subsurface Cu configurations, indicating that the catalytic enhancement originates predominantly from electronic structure modulation rather than geometric distortion.

While adsorption energetics and charge transfer describe intermediate stability, catalytic performance is ultimately governed by reaction kinetics. Therefore, activation barriers for key O–O bond cleavage reactions were evaluated.

3.2.3. *Reaction kinetics and pathway selectivity*

Activation energies for O_2 and OOH dissociation were calculated using the lowest-energy adsorption configurations identified above (Table 4). Cu-containing surfaces exhibit substantially lower reaction barriers than Au(111), with O_2 dissociation requiring only 0.189 eV on Cu(111) compared with 1.446 eV on Au(111). Similar trends are observed for OOH dissociation, confirming the strong ability of Cu-rich

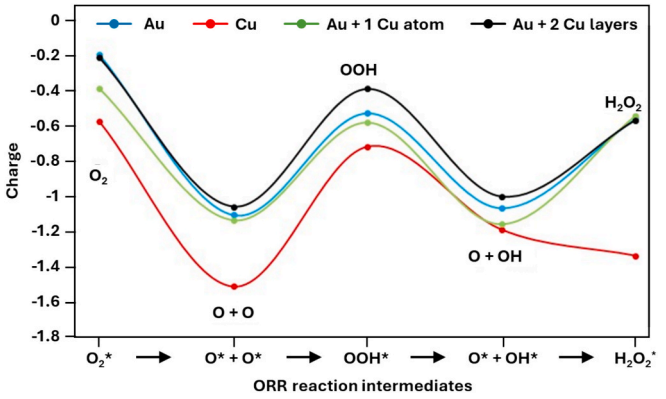

Fig. 3. Mulliken charge distribution on oxygen atoms across successive ORR intermediates (O_2*, O* + O*, OOH*, O* + OH*, and H_2O_2*) on Au, Cu, and Cu-modified Au(111) surfaces. Cu-containing surfaces exhibit greater charge transfer, promoting O–O bond activation, whereas Au-rich surfaces stabilise less perturbed intermediates. This charge modulation underpins selective ROS generation at Cu-Au interfacial sites.

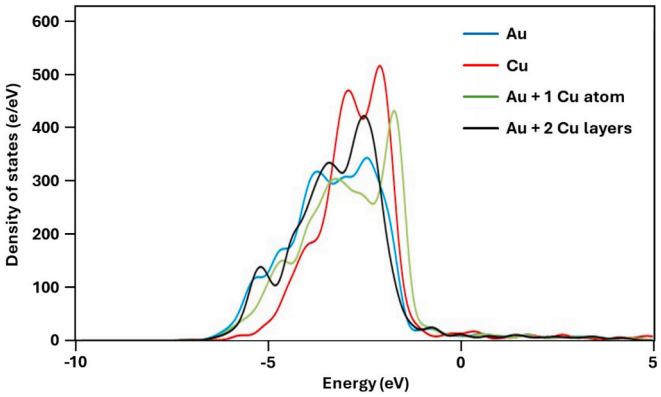

Fig. 4. D-projected density of states (pdos) for surface atoms of au, cu, and cu-modified au(111). cu incorporation shifts the d-band centre toward the Fermi level, increasing adsorption strength and catalytic activity. This electronic modulation enables efficient oxygen activation while maintaining selectivity toward ROS-generating intermediates at Cu-Au interfaces.

Table 3
Lattice constants of Au, Cu, and Cu-modified Au(1 1 1) surfaces. Minor lattice contraction upon Cu incorporation indicates that catalytic enhancement is dominated by electronic effects rather than structural distortion, consistent with interfacial charge-transfer-driven activity.

Surface	Lattice constant (a, b (Å))
Au(111)	5.94
Cu(111)	5.08
Au(111) + 1 Cu layer	5.94
Au(111) + 2 Cu layers	5.80

Table 4
Activation energies (eV) for O_2 and OOH dissociation on Au, Cu, and Cu-modified Au(111) surfaces. Cu-containing surfaces exhibit reduced barriers, enabling rapid O–O bond cleavage, while Au-containing environments stabilise intermediates. This balance supports selective H_2O_2 formation and sustained ROS generation at Cu-Au interfacial sites.

Reaction	Au	Cu	Au + 1 Cu layer	Au + 2 Cu layers
$O_2^* \rightarrow O^* + O^*$	1.446	0.189	0.700	1.418
$HOO^* \rightarrow HO^* + O^*$	0.522	0.021	0.502	0.837

domains to promote O–O bond cleavage.

The calculated activation energies are in good agreement with reported literature values [29,30,48–50], supporting the validity of the computational framework. Together with the thermodynamic and electronic structure analyses, these results indicate that Cu-rich sites provide kinetically favourable pathways for oxygen activation, whereas Au-rich environments moderate reactivity by stabilising partially reduced intermediates. This balance favours selective H_2O_2 formation rather than complete reduction to water, promoting sustained ROS precursor generation. The predicted reaction pathway is consistent with the enhanced Cu^{2+} release and antibacterial performance of $CuAu_{1.5}$ reported in the Cu^{2+} release measurements (Section 3.3) and antibacterial assays (Section 3.5), respectively.

Collectively, the DFT calculations predict that Cu-Au catalytic interfaces promote oxygen activation, selective H_2O_2 generation, and interfacial electron transfer. To determine whether these computationally predicted mechanisms are realised experimentally, electrochemical stability, H_2O_2 generation, and Cu^{2+} release measurements were subsequently performed.

3.3. Experimental validation of interfacial catalysis

3.3.1. Electrochemical stability and H_2O_2 generation

To verify whether the catalytic mechanisms predicted by DFT are realised experimentally, electrochemical stability and oxygen reduction measurements were performed. These experiments provide direct evidence for sustained catalytic activity and ROS precursor generation at the Cu-Au catalytic interfaces identified experimentally in Section 3.1 and analysed computationally in Section 3.2.

Chronoamperometric measurements demonstrate the operational durability of the Cu-Au core-nanocluster system under continuous electrochemical conditions (Fig. 5a). The catalyst retained approximately 84% of its initial current after 10 h of operation, indicating good electrochemical durability and preservation of catalytic activity. Although this result does not represent long-term storage stability, it confirms that the catalytic interfaces remain active during prolonged oxygen reduction.

RRDE measurements further provide direct experimental evidence for H_2O_2 generation during oxygen reduction (Fig. 5b). The measured H_2O_2 yield and electron transfer number indicate that oxygen reduction proceeds predominantly through a two-electron pathway, producing H_2O_2 as the principal ROS precursor. The direct detection of H_2O_2 experimentally validates the DFT-predicted preference for selective oxygen reduction at Cu-Au interfacial sites predicted by the DFT analyses in Sections 3.2.1-3.2.3, confirming that coupled Cu/Au domains favour ROS generation rather than complete reduction to water.

Collectively, the chronoamperometric and RRDE measurements confirm that Cu-Au catalytic interfaces remain electrochemically active during prolonged operation and promote selective H_2O_2 generation through a predominantly two-electron oxygen reduction pathway. These observations provide direct experimental validation of the adsorption energetics, charge-transfer behaviour, and reaction pathway selectivity predicted by the DFT calculations. Although H_2O_2 generation was directly verified, secondary ROS species such as •OH were not quantified experimentally and remain an important target for future investigation.

3.3.2. Galvanic corrosion and Cu^{2+} release

While the RRDE measurements confirm ROS precursor generation, galvanic coupling within the Cu-Au architecture is expected to simultaneously enhance Cu dissolution. To evaluate this process experimentally, Cu^{2+} release measurements were performed under O_2-saturated conditions using Cu, a physical mixture of Cu NPs and Au nanoclusters, and $CuAu_{1.5}$ (Table 5).

The inclusion of a physical mixture control provides a critical mechanistic validation by distinguishing true interfacial coupling from simple component coexistence. In NaCl solution, $CuAu_{1.5}$ exhibits substantially greater Cu^{2+} release than both pure Cu and the physical mixture, with release increasing from 21.33 to 138.67 μg/mL as electrolyte concentration increases. Although the physical mixture shows a modest increase relative to Cu alone, the significantly higher dissolution observed for $CuAu_{1.5}$ highlights the importance of intimate nanoscale Cu-Au junctions, consistent with the interfacial architecture identified in

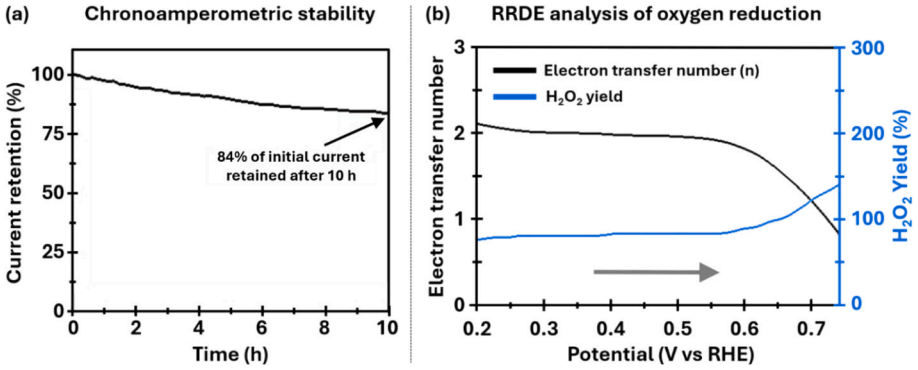

Fig. 5. Experimental validation of electrochemical durability and ROS precursor generation in Cu-Au core-nanocluster materials. (a) Chronoamperometric response recorded during 10 h of continuous operation, showing retention of approximately 84% of the initial current. (b) RRDE-derived electron transfer number (n) and H_2O_2 yield as a function of potential, confirming oxygen reduction through a predominantly two-electron pathway and direct H_2O_2 generation.

Table 5
Cu^{2+} release (μg/mL) and dissolved Cu (%) for Cu, Cu NPs + Au clusters, and $CuAu_{1.5}$ in O_2-saturated NaCl, HCl, and NaOH solutions. The enhanced dissolution of $CuAu_{1.5}$ relative to both pure Cu and the physical mixture confirms the role of Cu-Au interfacial coupling in promoting galvanic corrosion and Cu^{2+} release.

O_2-Saturated Solution	NaCl			HCl			NaOH
***Cu^{2+} Release* (μg/mL)**	**0.5 M**	**1.0 M**	**2.0 M**	**0.5 M**	**1.0 M**	**2.0 M**	**0.5 M**
Cu	0	0	0	1770.67	1845.33	1834.66	0
Cu NPs + Au clusters	3.56	9.69	15.45	1856.31	1943.71	1985.48	0
$CuAu_{1.5}$	21.33	85.33	138.67	2176.00	2346.67	2442.67	0
***Dissolved Cu* (%)**	**0.5 M**	**1.0 M**	**2.0 M**	**0.5 M**	**1.0 M**	**2.0 M**	**0.5 M**
Cu	0	0	0	53.12	55.36	55.04	0
$CuAu_{1.5}$	0.64	2.56	4.16	65.28	70.40	73.28	0

Section 3.1 and the ORR mechanism predicted by DFT in Section 3.2.

Under acidic conditions, Cu dissolution is further amplified, with $CuAu_{1.5}$ reaching 2442.67 μg/mL at 2.0 M HCl, corresponding to 73.28% dissolved Cu. This behaviour reflects proton-assisted corrosion coupled with galvanic electron transfer, where Cu acts as a sacrificial anode and Au functions as a cathodic oxygen reduction site. In contrast, no measurable Cu^{2+} release was observed in NaOH owing to surface passivation through hydroxide formation. These trends demonstrate that local chemical environments directly regulate interfacial electron transfer and dissolution kinetics.

The enhanced dissolution observed for $CuAu_{1.5}$ confirms that the catalytic interfaces promote both oxygen reduction and galvanic corrosion, establishing a cooperative mechanism for simultaneous ROS generation and Cu^{2+} release. Together with the RRDE measurements, these results provide direct experimental evidence that the superior activity of $CuAu_{1.5}$ originates from interfacial coupling rather than simple coexistence of Cu and Au components.

The combined electrochemical and dissolution data establish a direct structure–property-performance relationship. Structural characterisation confirmed the formation of abundant Cu-Au interfacial sites (Section 3.1), DFT calculations identified these sites as catalytically active centres for oxygen reduction (Section 3.2), and the present experiments verify both H_2O_2 generation and galvanically enhanced Cu dissolution. These coupled processes provide the mechanistic basis for the superior antibacterial performance of $CuAu_{1.5}$ reported in Section 3.5.

While galvanic corrosion and ROS generation represent the primary chemically driven antimicrobial pathways, plasmonic Au nanoclusters may provide an additional light-responsive contribution through photothermal enhancement. This possibility was therefore investigated using optical-thermal simulations.

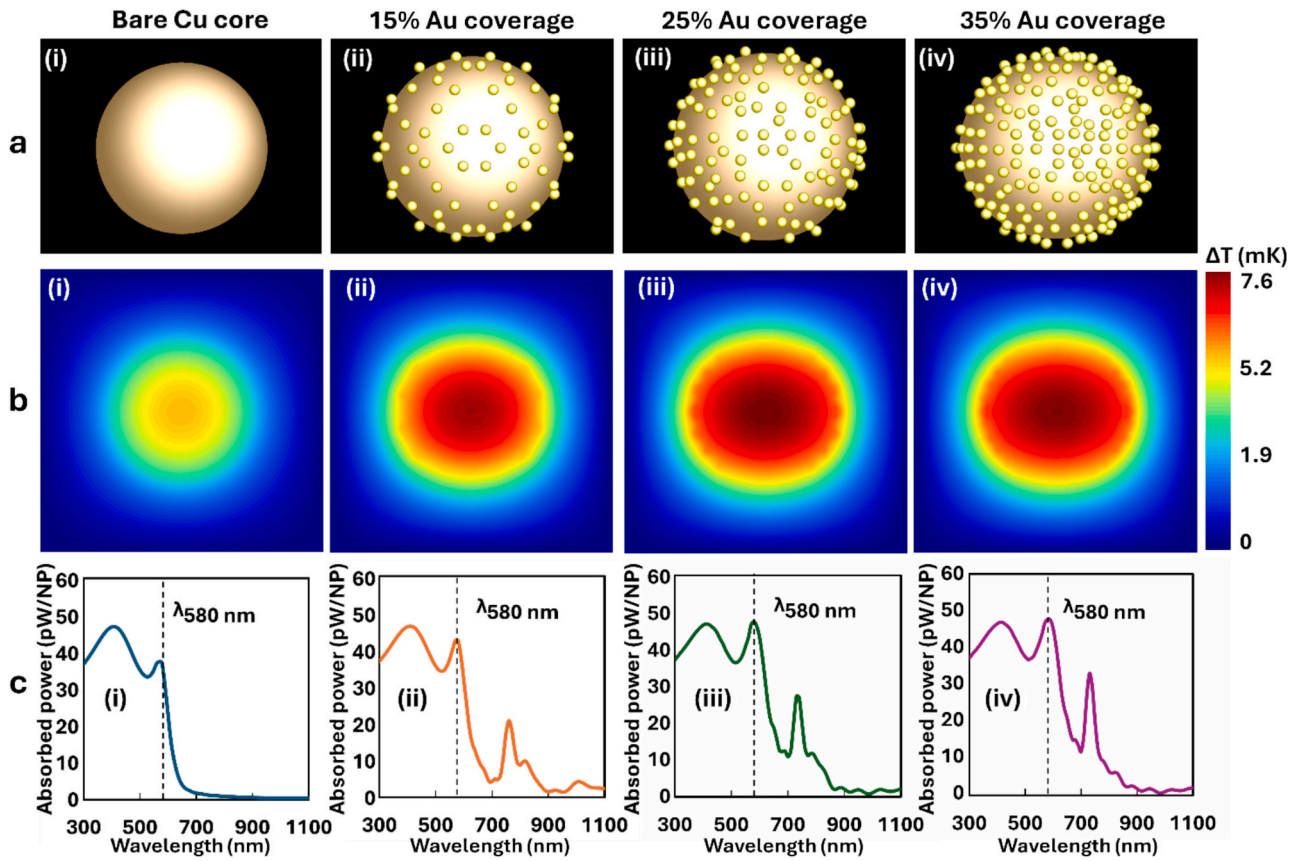

Fig. 6. Photothermal response of Cu-Au core-nanocluster NPs with varying Au surface coverage under λ = 580 nm irradiation (100 mW/cm^2, 25 °C). (a) Structural models with 0, 15, 25, and 35% Au coverage. (b) Corresponding temperature distributions showing enhanced and more localised heating with increasing Au content. (c) Absorbed power spectra demonstrating increased optical absorption with Au incorporation and a plateau beyond 25% coverage due to plasmonic coupling saturation. The 25% coverage configuration ($CuAu_{1.5}$) provides near-optimal photothermal performance with efficient Au utilisation.

3.4. Photothermal performance and plasmonic enhancement

3.4.1. Au coverage effects on Single-NP heating

The influence of Au coverage on photothermal performance was investigated under λ = 580 nm irradiation (100 mW/cm, 25 °C). As shown in Fig. 6a, Au nanoclusters are distributed as discrete plasmonic domains across the Cu core rather than forming a continuous shell. This morphology promotes localised electromagnetic coupling at multiple interfacial sites. Corresponding thermal maps (Fig. 6b) reveal progressively enhanced and more spatially confined heating with increasing Au coverage.

At the single-NP level, absorbed power increases from 37.05 pW for bare Cu to 47.70 pW at 35% Au coverage (Fig. 6c), corresponding to a temperature rise from 5.90 to 7.59 mK [51]. Although the absolute temperature increase remains modest, the relative enhancement demonstrates that Au incorporation improves optical absorption and photothermal conversion efficiency. The absorption spectra further indicate that the enhancement originates from the evolution and broadening of plasmonic modes rather than a simple increase in metallic volume.

A plateau is observed beyond 25% Au coverage, where additional Au provides only marginal gains in absorbed power. This behaviour is consistent with plasmonic coupling saturation and identifies 25% coverage, corresponding closely to the experimentally observed $CuAu_{1.5}$ morphology described in Section 3.1, as an efficient balance between photothermal performance and material utilisation.

3.4.2. Collective heating and plasmonic coupling

To assess collective photothermal behaviour, $CuAu_{1.5}$ was modelled as a 3 × 3 NP array with interparticle spacings of 100 and 200 nm (Fig. 7). At 200 nm spacing, the array exhibits a maximum temperature rise of 10.1 mK and a minimum temperature of 5.7 mK. Reducing the spacing to 100 nm increases the maximum temperature to approximately 15 mK while substantially improving thermal uniformity throughout the array.

The enhanced heating at smaller separations arises from stronger near-field plasmonic coupling, which increases collective absorption and local heat generation [52]. The low thermal conductivity of the PVDF substrate further promotes heat confinement, enabling local temperature accumulation [46]. These results demonstrate that photothermal performance is governed primarily by NP density and spatial arrangement rather than single-particle heating alone.

3.4.3. Macroscopic photothermal performance

At higher NP densities (Fig. 8), $CuAu_{1.5}$ is predicted to achieve temperatures approaching 40–60 °C at concentrations of 10^7-10^8 NPs/cm, substantially lower than those typically required for equivalent solid Au NPs [32]. This improved efficiency arises from the distributed plasmonic architecture, where multiple Au nanoclusters generate localised electromagnetic hotspots that collectively enhance light absorption and heat generation [53].

While Cu^{2+} release and ORR-driven ROS generation remain the dominant antimicrobial pathways established in Section 3.3, photothermal heating may provide an additional illumination-dependent

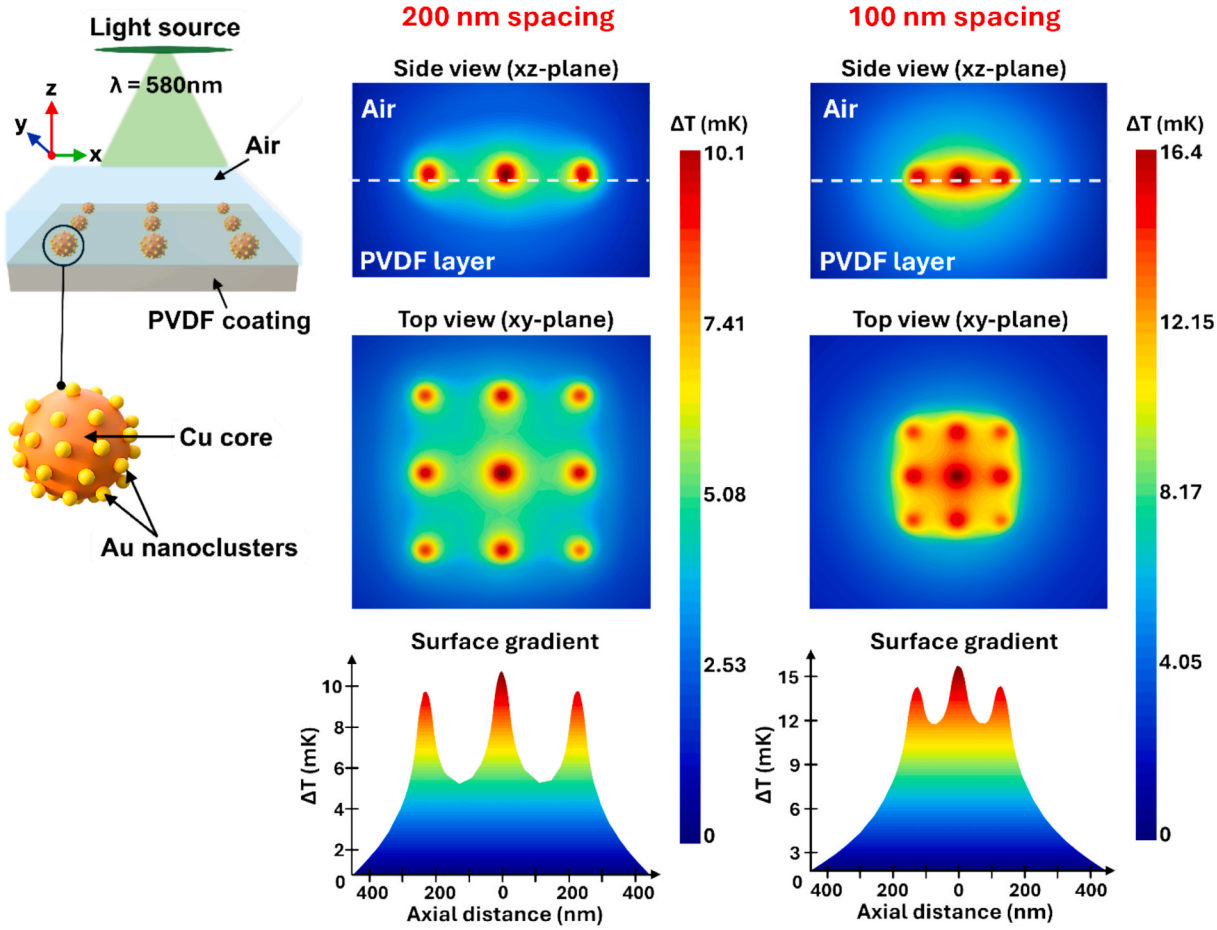

Fig. 7. Collective photothermal response of $CuAu_{1.5}$ NP arrays under optical excitation. Reducing the interparticle spacing from 200 to 100 nm increases the maximum temperature rise from 10.1 to approximately 15 mK and improves thermal uniformity across the array. Enhanced heating arises from stronger near-field plasmonic coupling and collective absorption at reduced separations, demonstrating that NP spacing and surface density play a dominant role in determining photothermal performance.

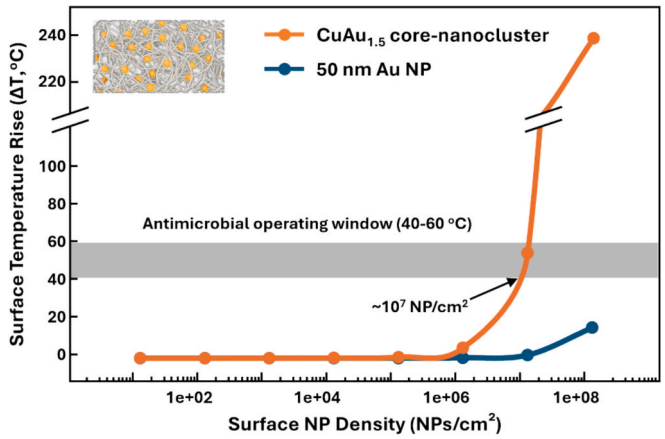

Fig. 8. Simulated surface temperature rise as a function of surface NP density under $\lambda = 580$ nm irradiation. $CuAu_{1.5}$ reaches the antimicrobial operating window (40–60 °C) at substantially lower densities than conventional Au NPs owing to enhanced absorption and hotspot generation arising from its distributed plasmonic nanocluster architecture. Inset: schematic representation of a PVDF-coated fibre network functionalised with $CuAu_{1.5}$ NPs.

enhancement by promoting membrane disruption and accelerating interfacial reaction kinetics [52,54,55].Beyond antimicrobial activity, the combined optical absorption and photothermal behaviour of the Cu-Au core-nanocluster architecture suggests broader potential for plasmon-enhanced catalytic systems, where localised heat generation may contribute to surface reaction enhancement under illumination.

3.5. Antimicrobial performance

3.5.1. Composition-Dependent activity

The antibacterial activity of Cu and $CuAu_x$ NPs (0.1 wt/v%, 1000 ppm) is shown in Fig. 9. Pristine Cu NPs, including all pre-treated variants, exhibit negligible inhibition against both *E. coli* and *S. aureus*, whereas all $CuAu_x$ systems display measurable antibacterial activity, confirming that Au incorporation activates a distinct antimicrobial mechanism beyond the intrinsic activity of Cu alone. A clear composition dependence is observed, with $CuAu_{1.5}$ exhibiting the largest inhibition zones (~1.0 cm for *E. coli* and ~ 1.4–1.5 cm for *S. aureus*), followed by $CuAu_1$, whereas $CuAu_2$ is less effective in its untreated form.

The reduced activity of $CuAu_2$ reflects excessive Au coverage, which partially shields Cu domains and limits both Cu^{2+} release and electron transfer for oxygen reduction. In contrast, $CuAu_1$ and $CuAu_{1.5}$ maintain an optimal balance between exposed Cu sites and catalytically active Au domains, maximising interfacial coupling and ROS generation. This interpretation is consistent with the interfacial architecture identified in Section 3.1, the ORR energetics predicted in Section 3.2, and the enhanced Cu^{2+} release experimentally verified in Section 3.3. The physical-mixture control further supports this mechanism, as the lower Cu^{2+} release observed for the Cu + Au mixture (Table 5) demonstrates that intimate nanoscale coupling, rather than simple component coexistence, is required to maximise antimicrobial activity.

S. aureus consistently exhibits greater susceptibility than *E. coli*, reflecting the absence of an outer membrane barrier and increased permeability to Cu ions and ROS [10]. Surface treatments further modulate activity, particularly for $CuAu_2$, where NaCl promotes initial Cu dissolution and PVP improves colloidal stability and dispersion. Together, these results demonstrate that antibacterial performance is governed primarily by Cu-Au interfacial design, with composition controlling the density of catalytically active junctions and surface treatment influencing reaction kinetics.

3.5.2. Physicochemical origins of antimicrobial activity

To further interpret the antibacterial behaviour, the physicochemical properties of the NPs were examined (Tables 6 and 7). Surface treatments produce only minor variations in hydrodynamic size and zeta potential, with no systematic correlation to antibacterial activity. In contrast, Au incorporation substantially increases particle size and reverses surface charge from positive to negative, confirming formation of the core-nanocluster architecture.

Despite this charge inversion, $CuAu_x$ NPs remain highly active whereas positively charged Cu NPs are largely inactive. This observation

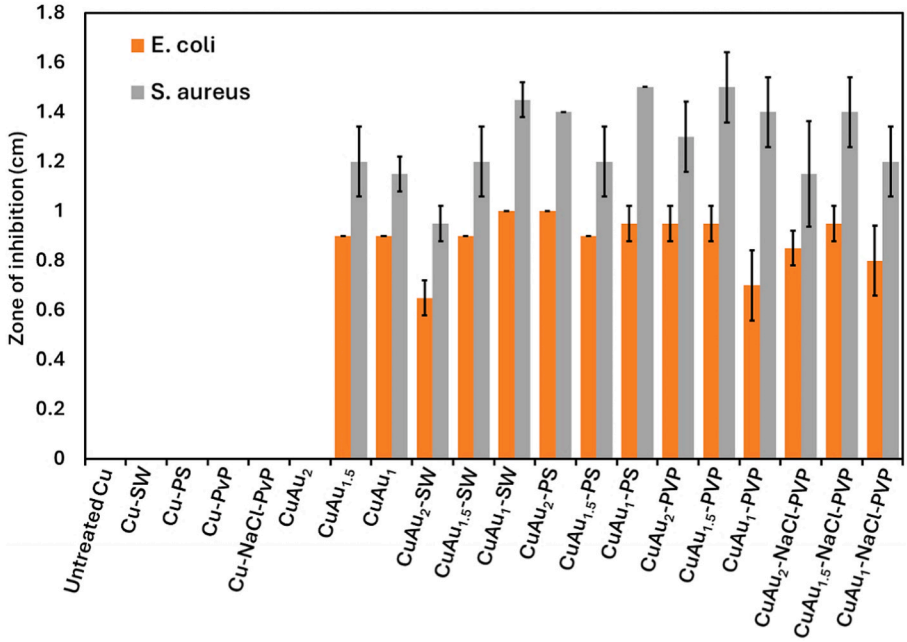

Fig. 9. Antibacterial activity of Cu and $CuAu_x$ NPs (0.1 wt/v%, 1000 ppm) against *S. aureus* and *E. coli*. Pristine Cu NPs exhibit negligible inhibition, whereas $CuAu_x$ systems show clear antibacterial activity, confirming the importance of Cu-Au interfacial coupling. $CuAu_{1.5}$ exhibits the highest inhibition, reflecting an optimal balance between exposed Cu domains and catalytically active Au nanoclusters. *S. aureus* is consistently more susceptible than *E. coli*, while NaCl and PVP treatments further enhance activity by promoting Cu dissolution and colloidal stability.

Table 6
Hydrodynamic size and zeta potential of Cu NPs under different treatments. Minor variations without correlation to activity indicate that surface treatment alone does not govern antimicrobial behaviour.

Treatment	Hydrodynamic size (nm)	Zeta potential (mV)
No treatment	386	31.7
Seawater	422.6	32.7
Saline (salt concentration)	369.7	37.3
PVP solution	429.9	29.1
NaCl and PVP solution	380.9	32.1

Table 7
Hydrodynamic size and zeta potential of Cu and $CuAu_x$ NPs. Au incorporation increases size and reverses charge, confirming core-nanocluster formation; activity despite negative charge indicates a non-electrostatic, ROS-driven mechanism.

Nanoparticle	Hydrodynamic size (nm)	Zeta potential (mV)
Cu	386	31.7
$CuAu_1$	915.9	−15.8
$CuAu_{1.5}$	591.9	−14.9
$CuAu_2$	435.8	−18.7

demonstrates that electrostatic interactions are not the dominant antibacterial mechanism. Instead, activity is governed primarily by chemically driven processes, namely galvanically enhanced Cu^{2+} release and ORR-mediated ROS generation. These findings are consistent with the H_2O_2 generation pathway experimentally verified in Section 3.3 and the ORR mechanism predicted by DFT in Section 3.2.

Together, the composition-dependent activity and physicochemical analysis establish that antimicrobial performance is controlled predominantly by interfacial catalytic processes rather than particle size or surface charge. The superior activity of $CuAu_{1.5}$ therefore originates from an optimal balance between accessible Cu sites, Au-mediated oxygen reduction, and a high density of catalytically active Cu-Au interfaces.

3.6. Structure-Property-Activity relationships

The combined experimental and computational results establish a direct structure–property-performance relationship for CuAu nanostructures. Structural characterisation (Section 3.1) confirmed the formation of abundant Cu-Au interfacial sites, while DFT calculations (Section 3.2) identified these interfaces as catalytically active centres for oxygen reduction and selective H_2O_2 generation. Electrochemical measurements (Section 3.3) subsequently validated enhanced Cu^{2+} release and a predominantly two-electron ORR pathway, providing direct experimental evidence for the proposed ROS-generation mechanism.

The superior antibacterial performance of $CuAu_{1.5}$ (Section 3.5) arises from an optimal balance between exposed Cu domains and catalytically active Au nanoclusters, maximising interfacial electron transfer and reaction kinetics. Although photothermal effects may provide an illumination-dependent enhancement at high NP densities (Section 3.4), antimicrobial activity is dominated by coupled Cu^{2+} release and ROS generation. Together, these findings identify interfacial engineering as the key strategy for optimising Cu-Au antimicrobial nanostructures.

4. Conclusion

This study demonstrates that the antimicrobial performance of CuAu core-nanocluster NPs is governed by interfacial coupling between Cu and Au domains rather than bulk composition alone. Structural characterisation confirmed the formation of abundant Cu-Au interfacial sites, while DFT calculations identified these interfaces as catalytically active centres for oxygen reduction, charge transfer, and selective H_2O_2 generation. Electrochemical measurements further validated a predominantly two-electron ORR pathway and enhanced Cu^{2+} release, providing direct experimental evidence for the coupled ROS-generation mechanism.

Among the compositions investigated, $CuAu_{1.5}$ exhibited the highest antibacterial activity, reflecting an optimal balance between exposed Cu domains and catalytically active Au nanoclusters. Photothermal simulations showed that plasmonic heating provides an illumination-dependent secondary enhancement, whereas Cu^{2+} release and ROS generation remain the dominant antimicrobial pathways under the conditions studied. Collectively, these findings identify interfacial engineering as the key design strategy for optimising Cu-Au antimicrobial nanostructures and provide a framework for the development of multifunctional antimicrobial coatings, filtration materials, and surface protection technologies, as well as future investigations of plasmon-enhanced catalytic systems in which optical absorption and photothermal effects contribute to enhanced interfacial reaction kinetics.

CRediT authorship contribution statement

Patrick Irigo: Writing – review & editing, Writing – original draft, Software, Methodology, Investigation, Formal analysis, Conceptualization. **Ya Li:** Validation, Investigation, Formal analysis. **Tong Liu:** Investigation, Data curation. **Etelka Chung:** Validation, Resources, Methodology, Formal analysis. **Yujia Luo:** Resources. **Xiangqun Zhuge:** Resources. **Miriam Roldán-Matilla:** Investigation. **Arisbel Cerpa-Naranjo:** Investigation. **Isabel Lado-Touriño:** Writing – review & editing, Supervision, Software. **Kun Luo:** Supervision, Funding acquisition. **María F. Gilsanz Muñoz:** Resources. **Guogang Ren:** Writing – review & editing, Supervision, Project administration, Funding acquisition.

Declaration of competing interest

The authors declare that they have no known competing financial interests or personal relationships that could have appeared to influence the work reported in this paper.

Acknowledgement

The authors gratefully acknowledge the supports from by the UK Royal Society (IEC\NSFC\201155), and the National Natural Science Foundation of China (No. 52474431).

Appendix A. Supplementary data

Supplementary data to this article can be found online at https://doi.org/10.1016/j.apsusc.2026.167591.

Data availability

Data will be made available on request.

References

[1] R. Li, / Rscpharma, S. K. Mondal, S. Chakraborty, S. Manna, and S. M. Mandal, "Antimicrobial nanoparticles: current landscape and future challenges," *RSC Pharmaceutics*, vol. 1, no. 3, pp. 388–402, Aug. 2024, doi: 10.1039/D4PM00032C.
[2] S. Fernando, T. Gunasekara, J. Holton, Antimicrobial Nanoparticles: applications and mechanisms of action, Sri Lankan Journal of Infectious Diseases 8 (1) (May 2018) 2, https://doi.org/10.4038/SLJID.V8I1.8167.
[3] J. Ramos-Zúñiga, N. Bruna, J.M. Pérez-Donoso, Toxicity mechanisms of copper nanoparticles and copper surfaces on bacterial cells and viruses, Int. J. Mol. Sci. 24 (13) (Jul. 2023) 10503, https://doi.org/10.3390/IJMS241310503.
[4] A.J. Huh, Y.J. Kwon, 'Nanoantibiotics': a new paradigm for treating infectious diseases using nanomaterials in the antibiotics resistant era, J. Control. Release 156 (2) (Dec. 2011) 128–145, https://doi.org/10.1016/J.JCONREL.2011.07.002.
[5] R. T. P. Da Silva, M. V Petri, E. Y. Valencia, P. H. C. Camargo, S. I. C. De Torresi, B. Spira, and A. Addresses, "Visible Light Plasmon Excitation of Silver Nanoparticles

Against Antibiotic-Resistant *Pseudomonas aeruginosa*," *bioRxiv*, p. 2020.01.10.902676, Jan. 2020, doi: 10.1101/2020.01.10.902676.
[6] W. Xie, S. Zhang, F. Pan, S. Chen, L. Zhong, J. Wang, and X. Pei, "Nanomaterial-based ROS-mediated strategies for combating bacteria and biofilms," *Journal of Materials Research 2021 36:4*, vol. 36, no. 4, pp. 822–845, Mar. 2021, doi: 10.1557/S43578-021-00134-4.
[7] K. Gold, B. Slay, M. Knackstedt, A.K. Gaharwar, Antimicrobial activity of Metal and Metal-Oxide based Nanoparticles, Adv. Ther. (weinh) 1 (3) (2018) 1700033, https://doi.org/10.1002/ADTP.201700033;PAGE:STRING:ARTICLE/CHAPTER.
[8] A.K. Chatterjee, R. Chakraborty, T. Basu, Mechanism of antibacterial activity of copper nanoparticles, Nanotechnology 25 (13) (2014) 135101, https://doi.org/10.1088/0957-4484/25/13/135101.
[9] M. Shi, H.S. Kwon, Z. Peng, A. Elder, H. Yang, Effects of surface chemistry on the generation of reactive oxygen species by copper nanoparticles, ACS Nano 6 (3) (Mar. 2012) 2157–2164, https://doi.org/10.1021/NN300445D.
[10] S. Moniri Javadhesari, S. Alipour, S. Mohammadnejad, and M. R. Akbarpour, "Antibacterial activity of ultra-small copper oxide (II) nanoparticles synthesized by mechanochemical processing against S. aureus and E. coli," *Materials Science and Engineering: C*, vol. 105, p. 110011, Dec. 2019, doi: 10.1016/J.MSEC.2019.110011.
[11] S.A. Olszowka, M.A. Manning, A. Barkatt, Copper Dissolution and Hydrogen Peroxide Formation in Aqueous Media, Corrosion 48 (5) (May 1992) 411–418, https://doi.org/10.5006/1.3315954.
[12] J.R. Conway, A.S. Adeleye, J. Gardea-Torresdey, A.A. Keller, Aggregation, Dissolution, and Transformation of Copper Nanoparticles in Natural Waters, Environ. Sci. Technol. 49 (5) (Mar. 2015) 2749–2756, https://doi.org/10.1021/ES504918Q.
[13] M. Roldán-Matilla, P. Irigo, M.L. Rojas-Cervantes, M.P. Arce, J. Pérez-Piñeiro, M. F. Gilsanz, I. Lado-Touriño, A. Cerpa-Naranjo, G. Ren, Structural characterisation and dynamic modelling of pegylated graphene oxide with Ag and Cu nanocluster, Appl. Surf. Sci. 688 (Apr. 2025) 162430, https://doi.org/10.1016/J.APSUSC.2025.162430.
[14] D. Chen, J. Li, Ultrasmall Au nanoclusters for bioanalytical and biomedical applications: the undisclosed and neglected roles of ligands in determining the nanoclusters' catalytic activities, Nanoscale Horiz. 5 (10) (Sep. 2020) 1355–1367, https://doi.org/10.1039/D0NH00207K.
[15] H. Chen, L. Zou, E. Hossain, Y. Li, S. Liu, Y. Pu, X. Mao, Functional structures assembled based on Au clusters with practical applications, Biomater. Sci. 12 (17) (Aug. 2024) 4283–4300, https://doi.org/10.1039/D4BM00455H.
[16] D. Cheng, R. Liu, K. Hu, Gold nanoclusters: Photophysical properties and photocatalytic applications, Front. Chem. 10 (Jul. 2022) 958626, https://doi.org/10.3389/FCHEM.2022.958626/XML/NLM.
[17] P. Rani, R.S. Varma, K. Singh, R. Acevedo, J. Singh, Catalytic and antimicrobial potential of green synthesized Au and Au@Ag core-shell nanoparticles, Chemosphere 317 (Mar. 2023) 137841, https://doi.org/10.1016/J.CHEMOSPHERE.2023.137841.
[18] S. Worakitjaroenphon, P. Shanmugam, S. Boonyuen, S. M. Smith, and K. Chookamnerd, "Green synthesis of silver and gold nanoparticles using Oroxylum indicum plant extract for catalytic and antimicrobial activity," *Biomass Conversion and Biorefinery 2023 15:19*, vol. 15, no. 19, pp. 25765–25776, Aug. 2023, doi: 10.1007/S13399-023-04734-4.
[19] K. Zheng, M.I. Setyawati, D.T. Leong, J. Xie, Antimicrobial Gold Nanoclusters, ACS Nano 11 (7) (Jul. 2017) 6904–6910, https://doi.org/10.1021/ACSNANO.7B02035.
[20] S. Thota, Y. Wang, J. Zhao, Colloidal Au–Cu alloy nanoparticles: synthesis, optical properties and applications, Mater. Chem. Front. 2 (6) (May 2018) 1074–1089, https://doi.org/10.1039/C7QM00538E.
[21] K. Luo, Y. Li, T. Liu, X. Zhuge, E. Chung, A.R. Timms, S.P. Graham, G. Ren, Functionalized Copper Nanoparticles with Gold Nanoclusters: Part I. Highly Selective Electrosynthesis of Hydrogen Peroxide, ACS Omega 8 (39) (Oct. 2023) 36171–36178, https://doi.org/10.1021/ACSOMEGA.3C03665/ASSET/IMAGES/LARGE/AO3C03665_0004.JPEG.
[22] A. Ma, J. Wang, Y. Wang, Y. Zuo, Y. Ren, X. Ma, S. Wang, Atomically precise M_{15} (M = Au/Ag/Cu) alloy nanoclusters: Structural analysis, optical and electrocatalytic CO_2 reduction properties, Polyoxometalates 3 (2) (Jun. 2024) 9140054, https://doi.org/10.26599/POM.2024.9140054.
[23] V. Viswanathan, H.A. Hansen, J. Rossmeisl, J.K. Nørskov, Unifying the 2e - and 4e - reduction of oxygen on metal surfaces, J. Phys. Chem. Lett. 3 (20) (Oct. 2012) 2948–2951, https://doi.org/10.1021/JZ301476W/SUPPL_FILE/JZ301476W_SI_001.PDF.
[24] S. Das, A. Mishra, M.M. Ghangrekar, Production of hydrogen peroxide using various metal-based catalysts in electrochemical and bioelectrochemical systems: mini review, J. Hazard. Toxic Radioact. Waste 24 (3) (Jul. 2020) 06020001, https://doi.org/10.1061/(ASCE)HZ.2153-5515.0000498.
[25] N. Wang, S. Jiang, X. Wang, R. Zhang, I.I.N. Etim, J. Duan, B. Hou, Highly Efficient Electrosynthesis of H2O2 by Heteroatom-Doped Carbon Nanosheets for In Situ Sterilization, ACS Appl. Nano Mater. 8 (42) (Oct. 2025) 20450–20462, https://doi.org/10.1021/ACSANM.5C03701.
[26] C. Zhang, P. Shan, Y. Zou, T. Bao, X. Zhang, Z. Li, Y. Wang, G. Wei, C. Liu, and C. Yu, "Stable and high-yield hydrogen peroxide electrosynthesis from seawater," *Nature Sustainability 2025 8:5*, vol. 8, no. 5, pp. 542–552, Apr. 2025, doi: 10.1038/s41893-025-01538-4.
[27] A. Zhang, J. Wu, L. Xue, C. Li, S. Zeng, D. Caracciolo, S. Wang, C.J. Zhong, Engineering active sites of gold-cuprous oxide catalysts for electrocatalytic oxygen reduction reaction, ACS Appl. Mater. Interfaces 13 (39) (Oct. 2021) 46577–46587, https://doi.org/10.1021/ACSAMI.1C11730.
[28] Y. Xie, Y. Yang, D.A. Muller, H.D. Abrunã, N. Dimitrov, J. Fang, Enhanced ORR Kinetics on Au-Doped Pt–Cu Porous Films in Alkaline Media, ACS Catal. 10 (17) (Sep. 2020) 9967–9976, https://doi.org/10.1021/ACSCATAL.0C02690.
[29] E. Sargeant, F. Illas, P. Rodríguez, F. Calle-Vallejo, Importance of the gas-phase error correction for O2 when using DFT to model the oxygen reduction and evolution reactions, J. Electroanal. Chem. 896 (Sep. 2021) 115178, https://doi.org/10.1016/J.JELECHEM.2021.115178.
[30] L.E.B. Lucchetti, M.O. Almeida, J.M. de Almeida, P.A.S. Autreto, K.M. Honorio, M. C. Santos, Density functional theory studies of oxygen reduction reaction for hydrogen peroxide generation on Graphene-based catalysts, J. Electroanal. Chem. 895 (Aug. 2021) 115429, https://doi.org/10.1016/J.JELECHEM.2021.115429.
[31] Z. Jiang, M. Li, T. Yan, T. Fang, Decomposition of H2O on clean and oxygen-covered Au (1 0 0) surface: a DFT study, Appl. Surf. Sci. 315 (1) (Oct. 2014) 16–21, https://doi.org/10.1016/J.APSUSC.2014.07.076.
[32] S. Yoo, S. W. Yoon, W. N. Jung, M. H. Chung, H. Kim, H. Jeong, and K. H. Yoo, "Photothermal inactivation of universal viral particles by localized surface plasmon resonance mediated heating filter membrane," *Scientific Reports 2022 12:1*, vol. 12, no. 1, pp. 1–12, Feb. 2022, doi: 10.1038/s41598-022-05738-2.
[33] K. Yue, J. Nan, X. Zhang, J. Tang, X. Zhang, Photothermal effects of gold nanoparticles induced by light emitting diodes, Appl. Therm. Eng. 99 (Apr. 2016) 1093–1100, https://doi.org/10.1016/J.APPLTHERMALENG.2016.01.077.
[34] P. Irigo, N. Yousif, I. Johnston, B. Tatarov, A. Yadav, E. Chung, K. Luo, G. Ren, Enhancing SERS Spectra through Surface-Doped Nanocluster Substrates: a Numerical Investigation of Plasmonic Silver Coated Pt and Pd Core-Shell-Satellite Structures, J. Phys. Chem. C (Oct. 2024), https://doi.org/10.1021/acs.jpcc.4c05229.
[35] H. Zhang, H.J. Chen, X. Du, D. Wen, Photothermal conversion characteristics of gold nanoparticle dispersions, Sol. Energy 100 (Feb. 2014) 141–147, https://doi.org/10.1016/J.SOLENER.2013.12.004.
[36] J.P. Perdew, Y. Wang, Accurate and simple analytic representation of the electron-gas correlation energy, Phys. Rev. B 45 (23) (Jun. 1992) 13244, https://doi.org/10.1103/PhysRevB.45.13244.
[37] B. Delley, From molecules to solids with the DMol3 approach, J. Chem. Phys. 113 (18) (Nov. 2000) 7756–7764, https://doi.org/10.1063/1.1316015.
[38] B. Delley, Ground-state enthalpies: Evaluation of electronic structure approaches with emphasis on the density functional method, J. Phys. Chem. A 110 (50) (Dec. 2006) 13632–13639, https://doi.org/10.1021/JP0653611/SUPPL_FILE/JP0653611SI20060818_115435.PDF.
[39] B. Delley, Hardness conserving semilocal pseudopotentials, Phys. Rev. B 66 (15) (Oct. 2002) 155125, https://doi.org/10.1103/PhysRevB.66.155125.
[40] J.S. Humphrey, R. Amin-Sanayei, "Vinylidene Fluoride Polymers," *Encyclopedia of Polymer*, Sci. Technol. (Jan. 2003), https://doi.org/10.1002/0471440264.PST392.
[41] R. Gillibert, F. Colas, M.L. de La Chapelle, P.G. Gucciardi, Heat Dissipation of Metal Nanoparticles in the Dipole Approximation, Plasmonics 15 (4) (Aug. 2020) 1001–1005, https://doi.org/10.1007/S11468-020-01128-4/METRICS.
[42] A.O. Govorov, W. Zhang, T. Skeini, H. Richardson, J. Lee, N.A. Kotov, Gold nanoparticle ensembles as heaters and actuators: Melting and collective plasmon resonances, Nanoscale Res. Lett. 1 (1) (Jun. 2006) 84–90, https://doi.org/10.1007/S11671-006-9015-7/METRICS.
[43] H.H. Richardson, M.T. Carlson, P.J. Tandler, P. Hernandez, A.O. Govorov, Experimental and theoretical studies of light-to-heat conversion and collective heating effects in metal nanoparticle solutions, Nano Lett. 9 (3) (Mar. 2009) 1139–1146, https://doi.org/10.1021/NL8036905/ASSET/IMAGES/MEDIUM/NL-2008-036905_0006.GIF.
[44] A.O. Govorov, H.H. Richardson, Generating heat with metal nanoparticles, Nano Today 2 (1) (Feb. 2007) 30–38, https://doi.org/10.1016/S1748-0132(07)70017-8.
[45] R.B. Ross, *Metallic Materials Specification Handbook*, Metallic Materials Specification Handbook (1992), https://doi.org/10.1007/978-1-4615-3482-2.
[46] R. Dallaev, T. Pisarenko, D. Sobola, F. Orudzhev, S. Ramazanov, T. Trčka, Brief Review of PVDF Properties and applications potential, Polymers (basel) 14 (22) (Nov. 2022) 4793, https://doi.org/10.3390/POLYM14224793.
[47] Y.A. Çengel, J.M. Cimbala, Fluid mechanics: fundamentals and applications, McGraw-Hill Higher Education, Boston, 2006, p. 956.
[48] F. Wang, C. Xia, S.P. De Visser, Y. Wang, How does the oxidation state of palladium surfaces affect the reactivity and selectivity of direct synthesis of hydrogen peroxide from hydrogen and oxygen gases? A density functional study, J. Am. Chem. Soc. 141 (2) (Jan. 2019) 901–910, https://doi.org/10.1021/JACS.8B10281/ASSET/IMAGES/LARGE/JA-2018-10281E_0006.JPEG.
[49] J.S. Jirkovský, I. Panas, E. Ahlberg, M. Halasa, S. Romani, D.J. Schiffrin, Single atom hot-spots at Au-Pd nanoalloys for electrocatalytic H 2O 2 production, J. Am. Chem. Soc. 133 (48) (Dec. 2011) 19432–19441, https://doi.org/10.1021/JA206477Z/SUPPL_FILE/JA206477Z_SI_001.PDF.
[50] J.L.C. Fajín, M.N.D.S. Cordeiro, F. Illas, J.R.B. Gomes, Influence of step sites in the molecular mechanism of the water gas shift reaction catalyzed by copper, J. Catal. 268 (1) (Nov. 2009) 131–141, https://doi.org/10.1016/J.JCAT.2009.09.011.
[51] N. Pazos-Perez, J.M. Fitzgerald, V. Giannini, L. Guerrini, R.A. Alvarez-Puebla, Modular assembly of plasmonic core–satellite structures as highly brilliant SERS-encoded nanoparticles, Nanoscale Adv. 1 (1) (Jan. 2019) 122–131, https://doi.org/10.1039/C8NA00257F.
[52] D. You, T. Chen, G. Liu, Multiphysics modeling of plasmonic photothermal therapy, Therm. Sci. Eng. Prog. 46 (2023) 102240, https://doi.org/10.1016/J.TSEP.2023.102240.
[53] S. Manrique-Bedoya, M. Abdul-Moqueet, P. Lopez, T. Gray, M. Disiena, A. Locker, S. Kwee, L. Tang, R.L. Hood, Y. Feng, et al., Multiphysics modeling of plasmonic photothermal heating effects in gold nanoparticles and nanoparticle arrays,

J. Phys. Chem. C 124 (31) (2020) 17172–17182, https://doi.org/10.1021/ACS.JPCC.0C02443/ASSET/IMAGES/LARGE/JP0C02443_0008.JPEG.

[54] Y. Ren, Y. Yan, H. Qi, Photothermal conversion and transfer in photothermal therapy: from macroscale to nanoscale, Adv. Colloid Interface Sci. 308 (Oct. 2022) 102753, https://doi.org/10.1016/J.CIS.2022.102753.

[55] M. Kim, J.H. Lee, J.M. Nam, Plasmonic photothermal nanoparticles for biomedical applications, Adv. Sci. 6 (17) (2019), https://doi.org/10.1002/ADVS.201900471.